Hindawi
Advances in Civil Engineering
Volume 2023, Article ID 8337511, 15 pages
https://doi.org/10.1155/2023/8337511

Research Article

Dynamic Response Analysis of Segmental Lining under Ground Shock: A Simplified Calculation Method

Shihao Wang[1], **Ke Wang**[1], **Yong Wang**[1], **Yi Liu**[1], **Zhongyuan Xu**[2] and **Shaoliu Liu**[3]

[1]*Department of architectural Engineering, Henan College of Transportation, Zhengzhou 450000, China*
[2]*Shanghai Research Institute of Building Sciences Co. Ltd., Shanghai 200032, China*
[3]*State Key Laboratory of Disaster Prevention & Mitigation of Explosion & Impact, Army Engineering University of PLA, Nanjing 210007, Jiangsu, China*

Correspondence should be addressed to Shihao Wang; wang.shihao99@outlook.com

Received 9 March 2023; Revised 19 June 2023; Accepted 27 June 2023; Published 22 September 2023

Academic Editor: Kumar Anupam

The tunnel lining segments are assumed to be rigid, and the tensile, compression, shear, and bending properties of the joints are considered. A simplified calculation method for the dynamic response of the structure under the ground shock is proposed, and its correctness is verified by comparing it with results from the finite element method. Using this method, the dynamic response of a subway tunnel lining is calculated, the change in joint force is studied, and the influence of the angle between the load and the center of the minimum segment and the wavelength–diameter ratio on the peak joint force is examined. The results indicate that under the ground shock, shallow tunnel lining is in the impulsive regime, and the force of segment joints is mainly compressed. As the wavelength–diameter ratio increases, the peak values of the lining top displacement and vertical deformation increase significantly, and the proportion of displacement and deformation caused by the inertial force gradually decreases. Sine and cosine functions can be used to preliminarily judge if the bending moment and radial force of the joint are too large or too small, so that the resistance of the lining to ground shock can be improved to a certain extent by setting the positions of lining joints reasonably.

1. Introduction

Compared to other events that are determined by statistics, such as wind and live load, ground shock on tunnel lining is less likely to occur. However, since urban underground transportation systems are efficient public facilities with concentrated personnel and potential for serious secondary disasters, it is crucial to conduct research on tunnel structure deformation and other issues caused by the ground shock.

The lining of a shield tunnel mostly consists of assembled segment structures. The annular segments are connected to the ring joint using fastening bolts, and the whole lining structure is connected by the longitudinal joints. Numerical simulation and simplified theoretical analysis are the main methods used to study the mechanical response of a shield tunnel segment lining structure under external blast loads. Ganbin et al. [1] conducted numerical simulations on a proposed shield tunnel and obtained the propagation law of explosion stress waves in soft soil, pressure at different points around the tunnel, and the time history curve of tunnel lining structure and acceleration based on the explosion equivalent settings. Muyu and Zhifang [2] established a finite element model of a shield tunnel under explosion loads based on the Wuhan Yangtze River Tunnel and analyzed the dynamic response of various parts of the shield tunnel lining structure when the middle–upper edge of the lane plate was exposed to contact explosion with different apertures. Yang et al. [3] studied the dynamic response of a shallow underground tunnel structure under different equivalent trinitrotoluene and blast load angles. Rashiddel et al. [4] analyzed the influence of different types of joints on the segment lining structure under explosion loads. De et al. [5] compared and analyzed explosion test data under 70 g acceleration with numerical simulation results, and the research results showed that the dynamic response of the tunnel lining structure was related to the covering depth and water depth.

The treatment of the segment joint is critical in the theoretical study of the mechanical properties of segment lining

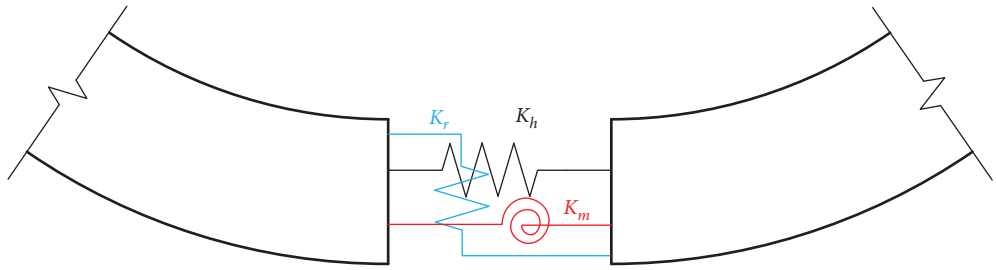

Figure 1: Schematic diagram of the spring model for the joint.

structures, and there are two approaches to it. The first method involves equivalenting the assembled lining structure to a continuous uniform structure. The influence of the segment joint is typically considered by multiplying the flexural stiffness of the tunnel lining by a reduction factor [6, 7]. The second method treats the joint as a special connection component called a hinge. The stiffness characteristics of the joint can be expressed using joint stiffness K, which includes rotational stiffness, axial stiffness, and shear stiffness [8–12]. Karinski and Yankelevsky [13] and Karinski et al. [14] simplified the segments into rigid bodies and considered the bending performance of the joint, and established the differential equation of the lining for solving,. Based on Karinski's model, Liu et al. [15] studied the effects of incident wave angle, segment thickness, and surrounding medium properties on the dynamic response of the lining structure under explosion seismic waves. Luo [16] used a composite spring to simulate the segment joint's tensile, compression, bending, and shear properties based on the same simplified model, established and solved the differential equations of motion for a multi-segment system, and obtained the displacement response law of the segment under internal explosion loads.

Based on the previous research results [13, 14], it has been observed that segment joints are the main areas of damage when the lining structure is subjected to external impact loads. This is due to the fact that the tensile, shear, and bending stiffness of the joint are much lower than those of a single segment. However, previous calculations in by Karinski and Yankelevsky [13] and Liu et al. [15] did not take into account the thickness of the segment, nor did they consider the circumferential tension (compression) and radial shear force at the joint of the segment. Taking these observations and real-life lining structures into consideration, the following assumptions are made in the simplified calculation model for the lining structure:

(1) The movement of the segments in the axial direction of the tunnel is disregarded, and they are assumed to move only in the plane under the external impact loads, which can be considered as a plane strain model.
(2) The segment is treated as a rigid body, and the deformation of a single segment is not considered. The motion of the segment is divided into translational motion and rotation around the center of mass.
(3) Springs are added to the joints of the segment in the circumferential, radial, and rotational directions to indicate the elastic–plastic relationship between the tension (pressure), tangential force, and bending moment of the joint, as well as the corresponding displacement.
(4) The tangential friction force of the surrounding medium on the lining structure is neglected.

2. Theoretical Model

The model of the lining structure is divided into two parts: the segment and the joint. The joint part of the structure is simplified as a zero-length elastoplastic spring in three directions. The segment is set as a rigid body, and its geometric dimensions, density, etc. are consistent with the lining structure in engineering.

2.1. Joint Model. Research data by Karinski and Yankelevsky [13], Karinski et al. [14], and De et al. [17] have demonstrated the feasibility of using the spring-hinge model to accurately calculate the mechanical response of segments. Based on the findings by Karinski and Yankelevsky [13], this study takes into account not only the rotational stiffness of the joint, but also the thickness of the segment, the circumferential tension (compression) stiffness of the joint, and the radial shear stiffness as shown in Figure 1. To represent the elastic–plastic relationship between the forces of the joint and the corresponding displacement, springs with zero length in the circumferential, radial, and rotational directions are, respectively, introduced.

The tensile stiffness of segment joint is mainly controlled by bolts. The numerical analysis of the tensile performance of segment joint was carried outby Luo [16], and the relationship between the circumferential force and the circumferential displacement at the joint was shown in Figure 2(a). In the figure, the O–H_0 segment with negative central displacement indicates compression of the region, while the positive circumferential displacement is divided into O–H_1 region, H_1–H_2 region, softening region, and residual strength region after H_2 point. In this model, the relationship between circumferential force and displacement of the joint under compression and deformation in the range of O–H_1 is simplified into linear elasticity, and the joint displacement will produce plastic deformation when the displacement exceeds H_1.

Based on the research results by Luo [16], it is assumed that the interaction force under radial shear is all generated by concrete deformation, and the relationship between the radial shear force and displacement of segment joints is

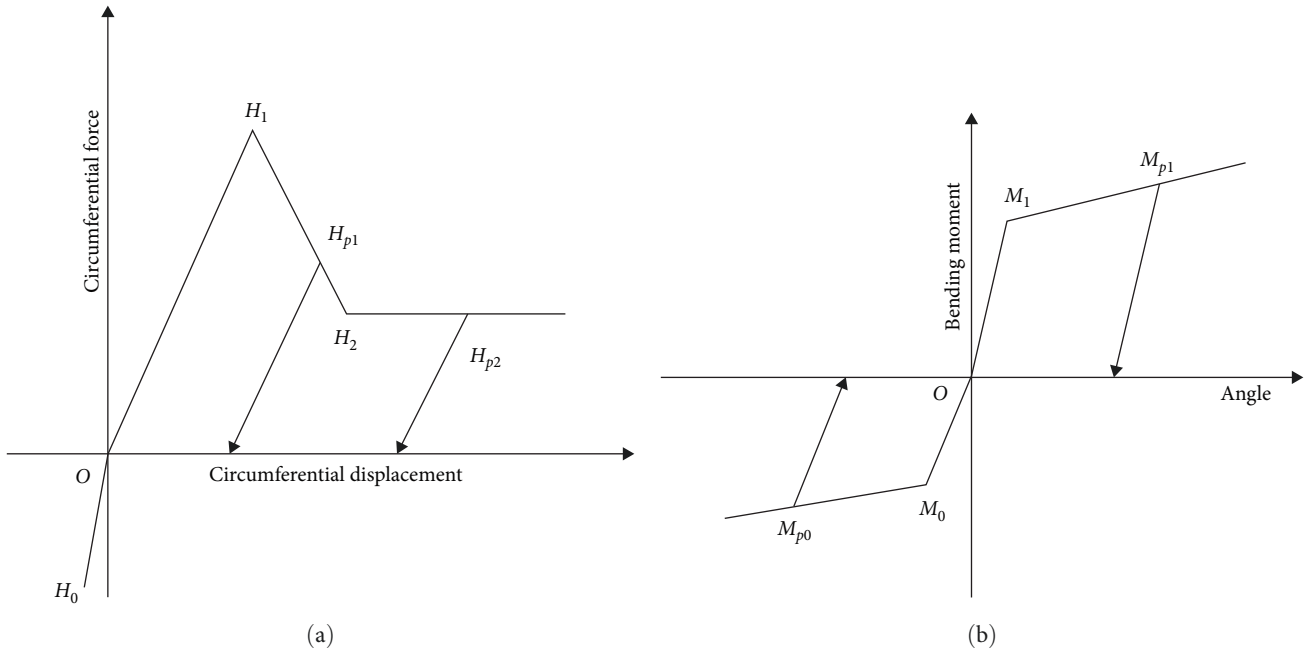

FIGURE 2: Circumferential and bending stiffness model of the joint: (a) circumferential force–displacement relationship and (b) bending moment–angle relationship.

simplified to linear elasticity, with a shear stiffness of K_r. The bending stiffness is determined according to the research results by Liu et al. [18], and the angle–moment curve is shown in Figure 2(b).

In order to express the circumferential force, radial force, and bending moment of the segment joint as a function of the circumferential and rotational displacement of the segment, it is essential to establish the relationship between the displacement of the segment and the circumferential, radial, and rotational displacement of the joint.

2.2. Segment Model. To establish the coordinate system, the origin was taken as the center of the lining structure, with the x-axis extending horizontally to the right and the y-axis extending vertically forward. The two ends of a single segment were labeled as A and B, respectively, in the clockwise direction. The strained condition of the ith segment is illustrated in Figure 3, where denotes the angle between end B of the ith segment and the x-axis, and θ_i represents the central angle of the ith segment. $F_{hi}^{(A)}$ and $F_{hi}^{(B)}$ represent the circumferential forces at ends A and B of the ith segment, while $F_{ri}^{(A)}$ and $F_{ri}^{(B)}$ represent the radial forces at ends A and B of the ith segment. Similarly, $F_{xi}^{(I)}$, $F_{yi}^{(I)}$, and $F_{mi}^{(\mathrm{I})}$ represent the bending moments at ends A and B of the ith segment. $F_{xi}^{(I)}$, $F_{yi}^{(I)}$, and $F_{mi}^{(\mathrm{I})}$, respectively, represent the horizontal force, vertical force, and bending moment on the segment centroid caused by the incident load on the ith segment, while $F_{xi}^{(G)}$, $F_{yi}^{(G)}$, and $F_{mi}^{(G)}$, respectively, represent the horizontal force, vertical force, and bending moment on the segment centroid caused by the surrounding medium on the ith segment.

The angle between the B end of the $(i+1)$th segment and the x axis is denoted as $\alpha_{i+1} = \alpha_i + \theta_i$. Therefore, the projection of the circumferential force and radial force at the joint

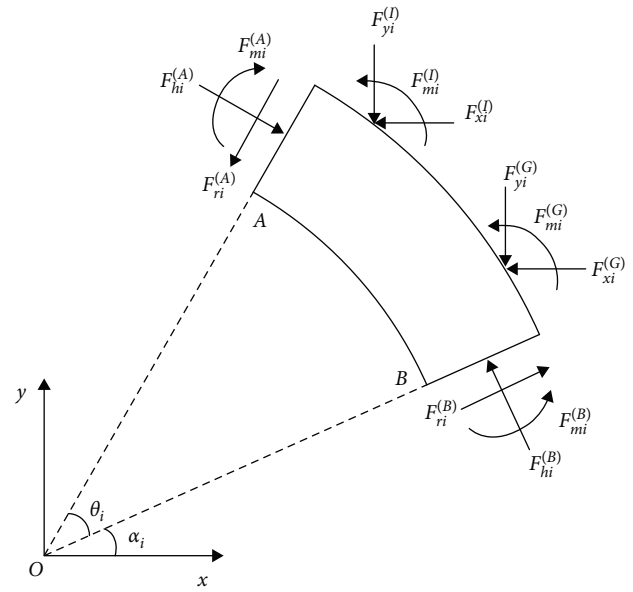

FIGURE 3: Schematic diagram of a single segment loading system.

of the two ends of the ith segment in the x direction can be expressed, respectively, as follows:

$$\begin{cases} F_{hix}^{(A)} = F_{hi}^{(A)} \sin(\alpha_{i+1}) \\ F_{hix}^{(B)} = -F_{hi}^{(B)} \sin(\alpha_i) \\ F_{rix}^{(A)} = -F_{ri}^{(A)} \cos(\alpha_{i+1}) \\ F_{rix}^{(B)} = F_{ri}^{(B)} \cos(\alpha_i). \end{cases} \quad (1)$$

The circumferential force and radial force at the joint of the two ends of the ith segment can be projected in the y direction as follows:

$$\begin{cases} F_{hiy}^{(A)} = -F_{hi}^{(A)}\cos(\alpha_{i+1}) \\ F_{hiy}^{(B)} = F_{hi}^{(B)}\cos(\alpha_i) \\ F_{riy}^{(A)} = -F_{ri}^{(A)}\sin(\alpha_{i+1}) \\ F_{riy}^{(B)} = F_{ri}^{(B)}\sin(\alpha_i). \end{cases} \tag{2}$$

To establish the motion equation of the ith segment, it is necessary to determine the centroid coordinates of the segment in order to calculate the bending moment caused by the circumferential and radial forces at the joint. Assuming uniform density distribution within the segment, the centroid angle of the ith segment is due to its symmetry. As the density is uniform, the centroid of the segment coincides with its center of mass. The distance between the center of mass and the center of the lining can be obtained as follows:

$$R_{ci} = \frac{4}{3}\frac{R_2^3 - R_1^3}{R_2^2 - R_1^2}\frac{\sin(\theta_i/2)}{\theta_i}, \tag{3}$$

where R_1 and R_2 represent the inner diameter and outer diameter of the lining, respectively.

To simplify the calculation of bending moment caused by circumferential force and radial force at the joint of the segment on the center of mass, it is observed from Figure 4 that the intermediate distance between the inner and outer diameters of the lining structure, denoted by D_i, and the angle between the projection of the radial force on the x–y plane and the x-axis, denoted by β_i, can be used to express the bending moment.

$$D_i = \sqrt{R_b^2 + R_{ci}^2 - 2R_bR_{ci}\cos(\theta_i/2)}, \tag{4}$$

$$\beta_i = \operatorname{across}\left(\frac{D_i^2 + R_b^2 - R_{ci}^2}{2D_iR_b}\right), \tag{5}$$

where R_b represents the distance between the center of the bolt cross-section at the segment joint and the origin O.

To calculate the bending moment of the circumferential and radial forces at the joints of the two ends of the ith segment on the center of mass of the segment, the intermediate distance D_i and angle β_i, as expressed earlier, can be used. Therefore, the bending moment can be calculated as follows:

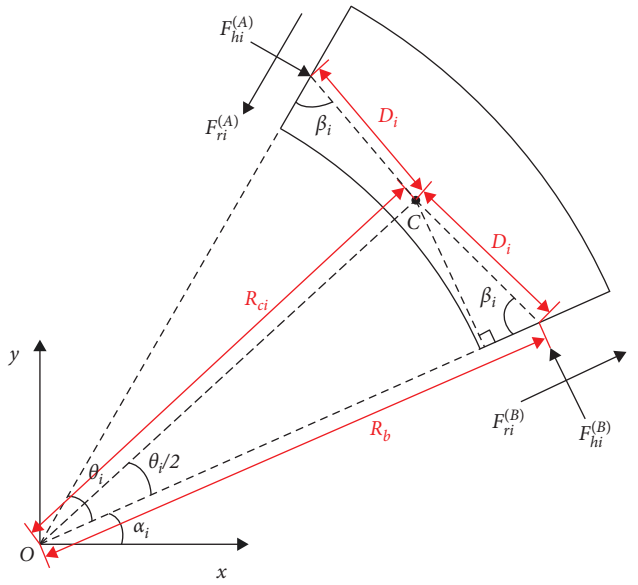

Figure 4: Schematic diagram of the distance between the joint and the center of mass.

$$\begin{cases} F_{him}^{(A)} = -F_{hi}^{(A)}D_i\cos(\beta_i) \\ F_{him}^{(B)} = F_{hi}^{(B)}D_i\cos(\beta_i) \\ F_{rim}^{(A)} = F_{ri}^{(A)}D_i\sin(\beta_i) \\ F_{rim}^{(B)} = F_{ri}^{(B)}D_i\sin(\beta_i). \end{cases} \tag{6}$$

Once these factors mentioned above have been determined, the motion equation of the ith segment can be established. This equation will take into account the forces and moments acting on the segment, as well as the segment's mass and moment of inertia. By solving this equation, it is possible to predict the behavior of the segment under the different conditions.

$$\begin{cases} m_i\ddot{u}_{xi} = F_{xi}^{(I)} + F_{xi}^{(G)} + F_{hix}^{(A)} + F_{hix}^{(B)} + F_{rix}^{(A)} + F_{rix}^{(B)} \\ m_i\ddot{u}_{yi} = F_{yi}^{(I)} + F_{yi}^{(G)} + F_{hiy}^{(A)} + F_{hiy}^{(B)} + F_{riy}^{(A)} + F_{riy}^{(B)} \\ I_i\ddot{u}_{mi} = F_{mi}^{(I)} + F_{mi}^{(G)} + F_{him}^{(A)} + F_{him}^{(B)} + F_{rim}^{(A)} + F_{rim}^{(B)} - F_{mi}^{(A)} + F_{mi}^{(B)} \end{cases}, \tag{7}$$

where m_i represents the mass of the ith segment, and I_i represents the moment of inertia of the segment with respect to the center of mass. $\ddot{u}_{xi}$, $\ddot{u}_{yi}$, and $\ddot{u}_{mi}$ represent the acceleration of the segment in x, y, and counterclockwise rotation direction about the center of mass, respectively.

The inertia I_i in Equation (7) of the segment can be calculated by:

$$I_i = \frac{\rho\theta_iL(R_2^4 - R_1^4)}{4} - \frac{\rho\theta_iL(R_2^2 - R_1^2)}{2}, \tag{8}$$

where ρ is the density and L is the width of the segment.

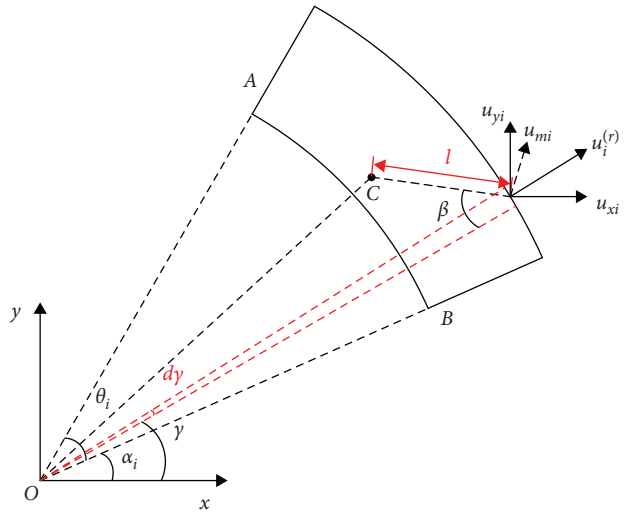

FIGURE 5: Schematic diagram of interaction force between structure and medium.

2.3. Interaction of Lining and Medium. The load on the structure includes not only caused by the incident load, but also caused by the movement of the structure under the ground shock. For each segment in the lining structure, the motion of each point on the outer surface of the segment is decomposed into circumferential motion and radial motion. Ignoring the friction on the contact surface between the structure and the medium and considering the radial motion of the points on the outer surface of the segment, the radial force on the structure is only related to its own wave impedance and the velocity of the segment. The motion decomposition and calculation diagram of the segment are shown in Figure 5.

The radial displacement of the segment can be expressed as the combination of the translation u_{xi} and u_{yi} of the segment and the rotational displacement u_{mi} around point C, which is the center of mass, as shown in Figure 5. Considering any element on the outer surface of the segment, its outer surface area is denoted as $R_2 d\theta L$, while the angle between the element and the x-axis is denoted as $d\gamma$, the angle between the line connecting the microelement and the center of mass and the line connecting the origin is denoted as γ, and the distance between the microelement and the center of mass is denoted as D. Thus, the radial displacement of the element can be calculated as follows:

The load on the structure includes not only the incident load, but also the reaction of the surrounding medium to the motion of the structure. For each segment in the lining structure, the motion of every point on its outer surface can be decomposed into circumferential and radial displacement. By neglecting friction on the contact surface between the structure and the medium, and taking into account the radial motion of points on the outer surface of the segment, the radial force on the structure depends solely on its own wave impedance and the velocity of the segment. The motion decomposition and calculation diagram of the segment is illustrated in Figure 5.

$$u_i^{(r)} = \begin{cases} u_{xi}\cos(\gamma) + u_{yi}\sin(\gamma) + u_{mi}l\sin(\beta)\gamma \le \alpha_i + \theta_i/2 \\ u_{xi}\cos(\gamma) + u_{yi}\sin(\gamma) - u_{mi}l\sin(\beta)\gamma > \alpha_i + \theta_i/2 \end{cases}, \tag{9}$$

where D and β are calculated from Equations (4) and (5).

$$l = \sqrt{R_2^2 + R_{ci}^2 - 2R_2R_{ci}\cos(\alpha_i + \theta_i/2 - \gamma)}, \tag{10}$$

$$\beta = \operatorname{across}\left(\frac{l^2 + R_2^2 - R_{ci}^2}{2lR_2}\right). \tag{11}$$

By integrating the outer surface of the entire segment in both the circumferential and radial directions, and considering the force of the medium on the segment in all directions, which can be calculated by Equation (12), the reaction of the surrounding medium to the motion of the structure can be obtained.

$$\begin{cases} F_{xi}^{(G)} = -\displaystyle\int_{\alpha_i}^{\alpha_i+\theta_i} \rho_s c_s \dot{u}_i^{(r)} \cos(\gamma) L R_2 d\gamma \\ F_{yi}^{(G)} = -\displaystyle\int_{\alpha_i}^{\alpha_i+\theta_i} \rho_s c_s \dot{u}_i^{(r)} \sin(\gamma) L R_2 d\gamma \\ F_{mi}^{(G)} = -\displaystyle\int_{\alpha_i}^{\alpha_i+\theta_i/2} \rho_s c_s \dot{u}_i^{(r)} l \sin(\beta) L R_2 d\gamma + \int_{\alpha_i+\theta_i/2}^{\alpha_i+\theta_i} \rho_s c_s \dot{u}_i^{(r)} l \sin(\beta) L R_2 d\gamma \end{cases}. \tag{12}$$

Equation (12) gives the force of the medium on the lining structure, where $\dot{u}_i^{(r)}$ is the radial velocity of the point on the outer surface of the segment. It is important to note that the interaction force can only be calculated when the segment moves toward the medium. When the segment and the medium move away from each other, the interaction force becomes zero. This algorithm implies that the medium and the structure exhibit identical motion under the incident loads. It takes into account the reaction force of the medium on the structure, while neglecting the adhesive effect between the medium and the structure.

3. Methodology

3.1. Differential Equation of Lining Motion. The analysis of the lining structure includes not only the incident load but

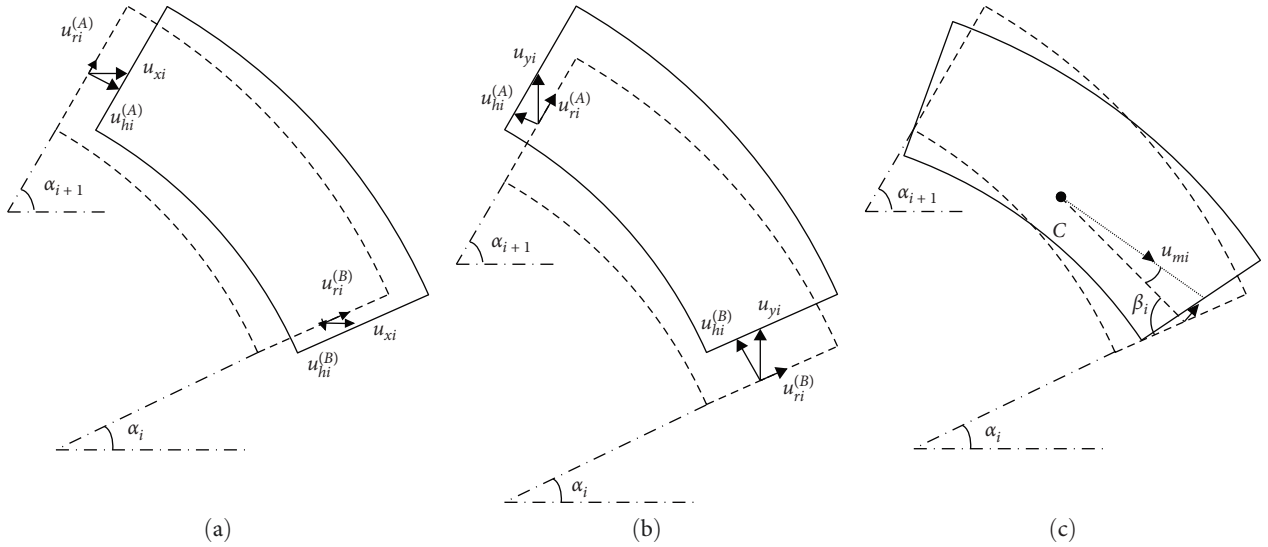

FIGURE 6: The joint displacement and segment displacement: (a) displacement in x direction of segment, (b) displacement in y direction of segment, and (c) rotation of segment.

also the interaction force between the structure and the medium. To establish the differential equation of motion for each segment, it is necessary to determine the relationship between the circumferential displacement, radial displacement, and rotation angle of the joint at both ends. By combining the relationship between force and displacement in three directions of the joint, the toroidal force, radial force, and bending moment at the joint can be obtained. Therefore, the differential equation of motion for the displacement of each segment can be established according to Equation (7) and solved using the Runge–Kutta method to obtain the mechanical response of the lining under the ground shock.

To simplify the calculation process, the displacement of the segment is decomposed into translation in the x and y directions and rotation around the center of mass, as shown in Figures 6(a)–6(c), respectively. The dotted line in the soil represents the initial position of the segment, and the solid line represents the position after the movement of the segment.

Since the circumferential force and radial force at the joint of the segment are dependent on the distance between the bolt holes of the two adjacent segments, the circumferential displacement, radial displacement, and rotation angle at the bolt holes of the joint can be expressed in terms of segment displacement shown in Figures 6 (a)–6(c), respectively:

$$\begin{cases} u_{hi}^{(A)} = u_{xi}\sin(\alpha_{i+1}) - u_{yi}\cos(\alpha_{i+1}) - 2D_i\sin(u_{mi})\cos(\beta_i - u_{mi}/2) \\ u_{ri}^{(A)} = -u_{xi}\cos(\alpha_{i+1}) - u_{yi}\sin(\alpha_{i+1}) + 2D_i\sin(u_{mi})\sin(\beta_i - u_{mi}/2), \\ u_{mi}^{(A)} = u_{mi} \end{cases} \tag{13}$$

$$\begin{cases} u_{hi}^{(B)} = -u_{xi}\sin(\alpha_i) + u_{yi}\cos(\alpha_i) + 2D_i\sin(u_{mi})\cos(\beta_i - u_{mi}/2) \\ u_{ri}^{(B)} = u_{xi}\cos(\alpha_i) + u_{yi}\sin(\alpha_i) + 2D_i\sin(u_{mi})\sin(\beta_i - u_{mi}/2) \\ u_{mi}^{(B)} = u_{mi} \end{cases}. \tag{14}$$

To express the force and displacement at the joints of each segment in the lining structure, we use the notation that the joint at the end A of the ith segment is referred to as the ith joint. The circumferential force and displacement of the joint are considered positive in terms of compression, the radial force and displacement are positive in terms of counterclockwise rotation of the joint, and the bending moment and angle are positive in terms of the inner opening of the segment. By combining the force analysis of a single segment shown in Figure 4 and Equations (13) and (14), we can derive the circumferential force, radial force and bending moment at the end A of the ith segment in a lining structure containing N segments:

$$\begin{cases} F_{hi}^{(A)} = K_h\left((u_{xi+1} - u_{xi})\sin(\alpha_{i+1}) + (u_{yi} - u_{yi+1})\cos(\alpha_{i+1}) + 2D_i\sin(u_{mi})\cos(\beta_i - u_{mi}/2) - 2D_{i+1}\sin(u_{mi+1})\cos(\beta_{i+1} - u_{mi+1}/2)\right) \\ F_{ri}^{(A)} = K_r\left((u_{xi} - u_{xi+1})\cos(\alpha_{i+1}) + (u_{yi} - u_{yi+1})\sin(\alpha_{i+1}) - 2D_i\sin(u_{mi})\sin(\beta_i - u_{mi}/2) - 2D_{i+1}\sin(u_{mi+1})\sin(\beta_{i+1} - u_{mi+1}/2)\right) \\ F_{mi}^{(A)} = K_m(u_{mi} - u_{mi+1}). \end{cases} \tag{15}$$

For a ring-shaped lining structure, the end B of the first segment corresponds to the end A of the Nth segment. Therefore, when calculating the force at the end A of the Nth segment, the displacement subscript $i+1$ in Equation (15) can be replaced with 1. Additionally, it can be observed that the force on the B end of the ith segment is equal to the force on the (i-1)th segment. Thus, based on Equation (15), the force on the end B of the ith segment can be expressed as follows:

$$\begin{cases} F_{hi}^{(B)} = K_h\left((u_{xi} - u_{xi-1})\sin(\alpha_i) + (u_{yi-1} - u_{yi})\cos(\alpha_i) - 2D_i\sin(u_{mi})\cos(\beta_i - u_{mi}/2)\right) + 2D_{i-1}\sin(u_{mi-1})\cos(\beta_{i-1} - u_{mi-1}/2) \\ F_{ri}^{(B)} = K_r\left((u_{xi-1} - u_{xi})\cos(\alpha_i) + (u_{yi-1} - u_{yi})\sin(\alpha_i) - 2D_{i-1}\sin(u_{mi-1})\sin(\beta_{i-1} - u_{mi-1}/2) - 2D_i\sin(u_{mi})\sin(\beta_i - u_{mi}/2)\right) \\ F_{mi}^{(B)} = K_m(u_{mi-1} - u_{mi}), \end{cases} \tag{16}$$

When calculating the force at B end of the first segment according to the above formula, the subscript of displacement $i-1$ should be changed to N.

3.2. Load on Structure. The load caused by an above–ground nuclear explosion can be simplified as a triangular load, with a wavelength of $L = H/2$, a rising time of $t_r = H/(6c_s)$, and a positive pressure time of $t_d = H/(2c_s)$, as shown by Hao [19]. Here, H represents the depth at which the structure is buried, and c_s is the compression wave velocity in the soil.

The peak pressure at depth h can be calculated as follows:

$$P_m(h) = P_{m0}\left(1 - \frac{(1 - c_1^2/c_0^2)h}{2c_1 t_+}\right), \tag{17}$$

where c_0 is elastic wave velocity, c_1 is plastic wave velocity, and P_{m0} is the peak surface pressure.

The pressure peak at any point depth x on the outer surface of the lining can be calculated by P_{mx} as follows:

$$P_{mx} = P_m(x)(\sin^2(\alpha_1 - \alpha_2)/K_\sigma + \cos^2(\alpha_1 - \alpha_2)), \tag{18}$$

where $P_m(x)$ is the peak pressure at depth $h = x$, α_1 is the incident load angle, α_2 is the angle between the vertical axis and the normal line of the lining surface at the depth of x, and K_σ is the lateral pressure coefficient. The load curve of any point on the outer surface of the lining can be expressed as follows:

$$P(x,t) = \begin{cases} t/t_r P_{mx} t < t_r \\ \dfrac{t_d - t}{t_d - t_r} P_{mx} t_r \le t \le t_d \\ 0 t > t_d \end{cases}. \tag{19}$$

To obtain the dynamic response of the lining under ground shock, $3N$ second-order total differential equations about the displacement of each segment were derived by substituting Equations (1), (2), (6), (12), (15), and (16) into Equation (7). These equations were then solved using the Runge–Kutta method. In each tiny time step, the load on each point of the structure is calculated according to Equation (19), and the load on each segment is obtained by integration, so as to solve the motion of the structure. This theoretical method can solve the dynamic response, rather than just the maximum values of structural deformation and displacement, of different forms of segmental lining structures with different diameters, segment thicknesses, segment curvatures under shock wave as long as the parameters of the segments, joints, surrounding media, and loads are known.

4. Results and Discussion

Usually, the lining of a shield tunnel is assembled by several rings with larger radii and one capping ring with a smaller radius. Based on a subway tunnel, differential equations of motion of the structure under ground shock are established according to its lining size and the material parameters. The initial conditions are expressed by Equation (20). The geometric dimensions of the lining are shown in Figure 7, and $P(t)$ in the figure is calculated according to Equation (19).

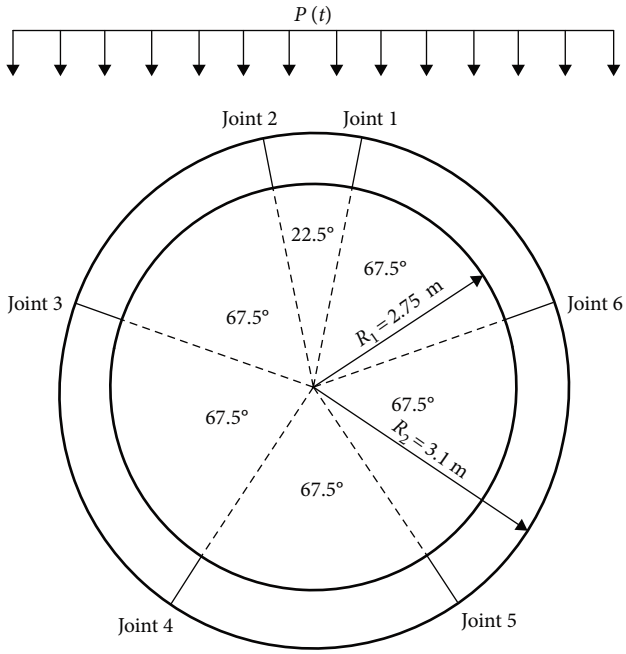

Figure 7: Schematic diagram of lining structure.

$$\begin{cases} u_{xi}\,(t=0) = u_{yi}\,(t=0) = u_{mi}\,(t=0) = 0 \\ \dfrac{d}{dt}u_{xi}\,(t=0) = \dfrac{d}{dt}u_{yi}\,(t=0) = \dfrac{d}{dt}u_{mi}\,(t=0) = 0. \end{cases} \tag{20}$$

The circumferential, radial, and bending stiffness coefficients of segment joints were determined by Luo [16] and Liu et al. [18], and the corresponding values in Figure 2 are shown in Table 1.

In Figure 2(a), the circumferential force corresponding to the elastic deformation limit H_1 is 160 kN, and corresponding to the initial residual strength H_2 is 50 kN. In Figure 2(b), the positive bending moment corresponding to the elastic deformation limit M_1 is 5.78×10^5 N·m, the negative bending moment corresponding to the elastic deformation limit M_0 is 6.8×10^5 N·m. A program is written to update the circumferential displacement and velocity of the joint at each calculation step, and the circumferential force of the joint is calculated through the displacement and velocity.

4.1. Model Verification. To verify the accuracy of the theoretical model and programing, a finite element model corresponding to Figure 7 was established. The model consists of rigid body segments and discrete beams to simulate the joints between segments. The stiffness coefficients of the discrete beams for circumferential, radial, and bending deformation were set according to Table 1. The structure was assumed to be located in saturated soil with a density of 1740 kg/m^3 and a compression wave velocity of 490 m/s [20]. To simulate the effect of soil on the structure, normal damping of 8.53×10^5 N·s/m was set on the outer surface of the structure in Equation (12). However, since the damping in the finite element cannot simulate the contact between the structure and the soil in a certain direction, the viscous force between the soil and the structure when they are separated was considered in Equation (12) during the calculation of the interaction between the soil and the structure in the theoretical calculation.

Table 1: Coefficients of spring stiffness of joint.

Spring type	Different stages	Stiffness coefficient
Circumferential spring	K_{O-H0}	1.47×10^{10} N·m^{-1}
	K_{O-H1}	1.16×10^{8} N·m^{-1}
	K_{H1-H2}	-1.16×10^{8} N·m^{-1}
Radial spring	K_r	1.28×10^{9} N·m^{-1}
Bending spring	K_{O-M1}	1.25×10^{8} N·m·rad^{-1}
	K_{M1-Mp1}	1.62×10^{7} N·m·rad^{-1}
	K_{O-M0}	1.28×10^{8} N·m·rad^{-1}
	K_{M0-Mp0}	8.29×10^{6} N·m·rad^{-1}

In the finite element model, the joint model is chosen as NONLINEAR_PLASTIC_DISCRETE_BEAM with zero length to correspond with the theoretical solution model. The segment model uses solid elements and the material is modeled as RIGID with a density consistent with that of concrete used in engineering. Contact between segments is not calculated. Since the surrounding medium material cannot be set as a rigid body and the contact between rigid and nonrigid bodies in finite element analysis would cause errors in the model, damping is added to the nodes on the outer surface of the segments in the finite element model. The value of the damping is equal to the product of the medium density and wave speed, which allows this model to correspond well with the theoretical solution model. In terms of loading conditions, in the theoretical solution, the load size and position on each segment are calculated at each $dt = 0.01$ ms time interval based on the medium wave speed and position of the outer surface of the segment. The total load on each segment at that time point is then obtained by integration to calculate the dynamic response of the segment. In the finite element model, each hexahedral element on the segment is divided into ~2 mm sides. The loading curve for each element on the outer surface of the segment is determined based on its position and medium wave speed.

Both the finite element software and theoretical calculation were used to solve the dynamic response of a 0.6 m thick structure under the ground shock with peak load $P_m = 300$ kPa, rise time $t_r = 6.7$ ms, and duration time $t_d = 20$ ms. By comparing the circumferential force, radial force, and bending moment of any joint, the accuracy of the calculation method and the program can be verified. The modified No. 5 joint in Figure 7 was selected, and the comparison of finite element and theoretical results is shown in Figure 8.

The comparison of results between the theoretical calculation and the finite element simulation for the circumferential force of No. 5 joint is shown in Figure 8. It can be observed that the results obtained from the finite element simulation are in good agreement with the theoretical calculation. The theoretical calculation yields slightly smaller

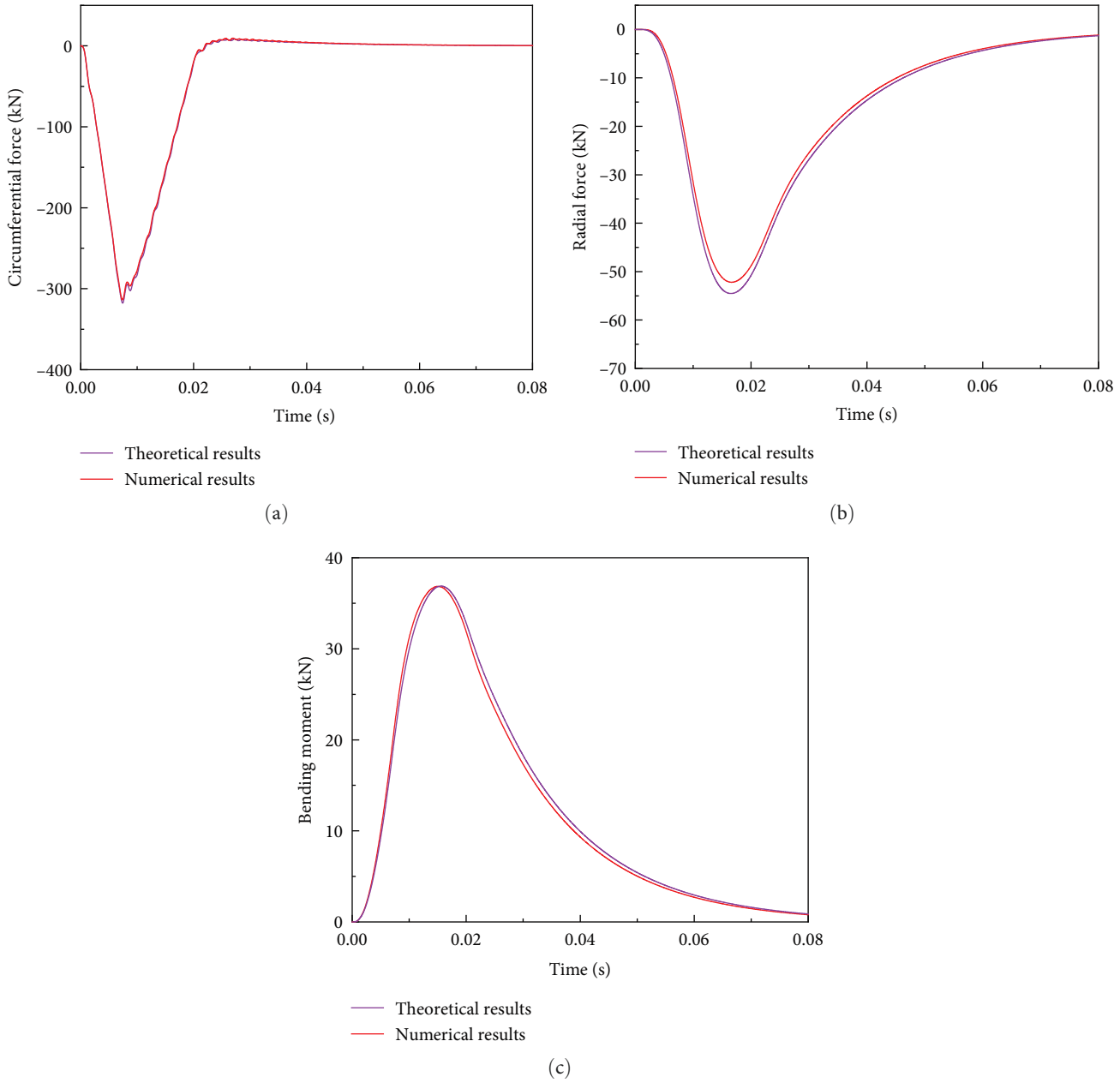

Figure 8: Comparison of finite element and theoretical results: (a) circumferential force–time curves, (b) radial force–time curves, and (c) bending moment–time curves.

values for the radial force and bending moment than the finite element simulation, but both methods show good agreement. By analyzing the data in Figure 8, it is found that the relative error of the maximum circumferential force of No. 5 joint is 1.3% in in Figure 8(a), the relative error of the maximum radial force is 4.2% in in Figure 8(b), and the relative error of the maximum bending moment is 0.1% in in Figure 8(c), with only a slight difference in the time to reach the peak bending moment. Therefore, the theoretical model and program established in this paper are capable of calculating the dynamic response of the structure under ground shock within a small error range.

4.2. Joint Forces. In this section, we consider the interaction between the structure and the surrounding medium in practical engineering. The interaction force is only considered when the segment moves toward the medium, and is set as zero when the segment and the medium are separated. Based on these considerations, we calculated the working conditions shown in Figure 7 and plotted the force–time curves of the joint circumferential force, radial force, and bending moment in Figure 9.

In Figure 9, it can be observed that the forces of each joint return to zero after the duration of the load. Due to the structure and load symmetry, the circumferential pressure

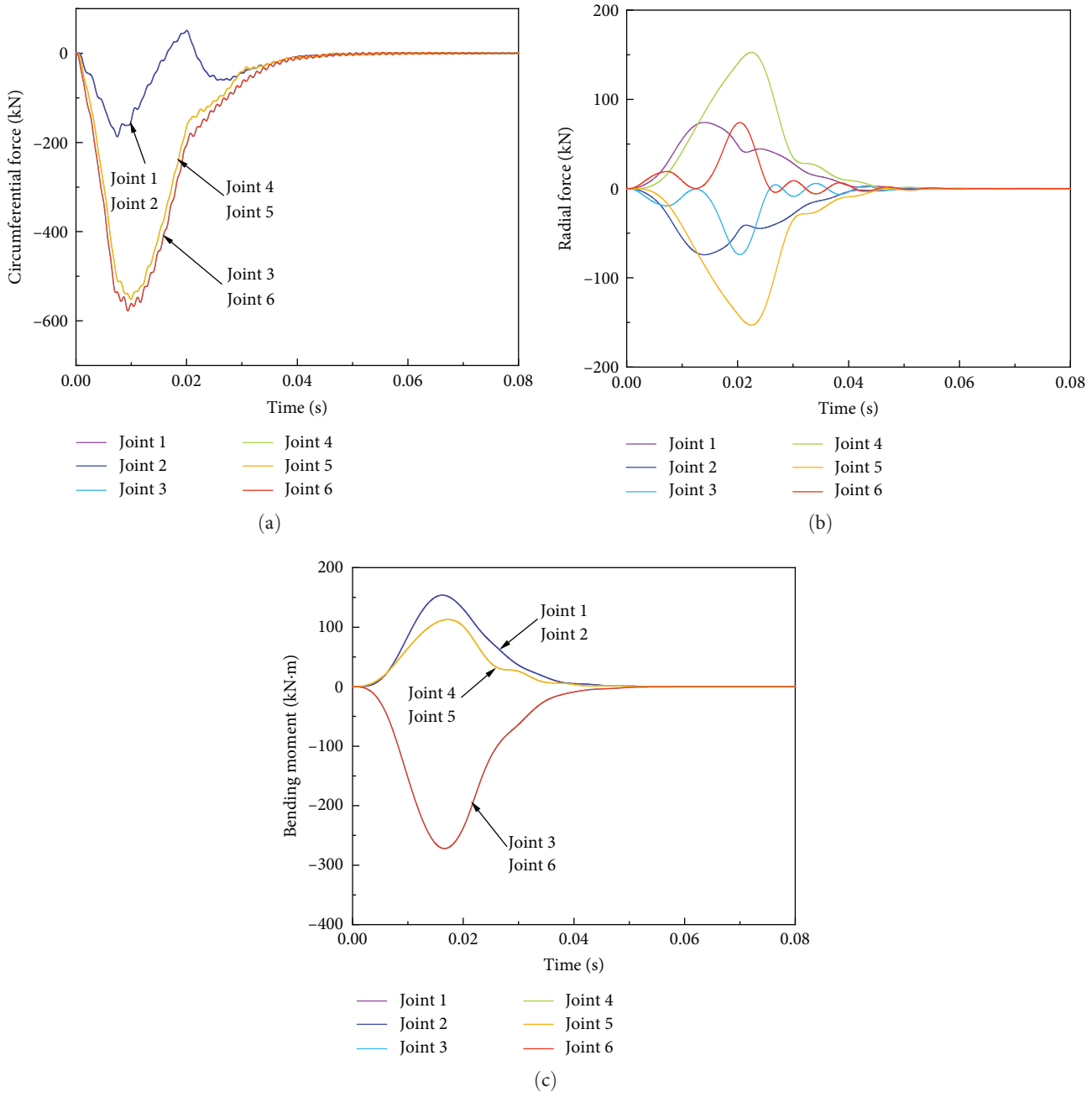

Figure 9: Time history curve of segment joint force: (a) circumferential force of joints, (b) radial force of joints, and (c) bending moment of joints.

and bending moment of joints 1 and 2, 3 and 6, 4 and 5 coincide with three curves, respectively. In Figure 9(a), the circumferential force of joints is mainly compression, and the circumferential pressure of joints 3–6 is similar, both of which are much larger than the circumferential force of joints 1 and 2. The time–history curve of the circumferential pressure of joints shows an obvious abrupt change after the end of the load. In Figure 9(b), joints 1 and 2 at both ends of the sealing ring reach their radial shear peaks first, followed by joints 3 and 6, and finally joints 4 and 5 that are not directly subjected to the load. However, the maximum radial shear peaks occur at joints 4 and 5. In Figure 9(c), all joints reach their peak bending moment before the end of the load. Joints 3 and 6 are negatively bent, while the other joints are positively bent. All the joint forces return to zero at about 2.5 times the duration of the load. Through the above analysis, it can be concluded that under the action of ground shock, the bending moment and circumferential force of the lining structure are controlled by joints 3 and 6 within the direct action range of the load, while the maximum radial force appears at joints 4 and 5, which are not directly affected by the load.

4.3. Influence of Incidence Load Angle. In practical engineering, linings are often assembled using split–joints in the direction of the tunnel length, which results in a nonzero angle between the load direction and the center of the sealing ring of the lining. As a result, the mechanical response of the structure is different from the results mentioned above. In Figure 7, the load acting on the structure from the top of the sealing ring is considered a forward incidence condition. The anticlockwise rotation angle in the direction of the incident load is defined as the incidence angle, and the motion of the segment and the dynamic response of the joint under different incidence angles are solved. Previous studies, such as the study byKarinski and Yankelevsky [13] and Liu et al. [15], have made dynamic analyses of the lining structure considering the bending stiffness of segment joints, and have found that different incidence angles have a significant influence on the internal forces and deformations of joints. By comparing the data in Figure 9, it is apparent that the maximum forces of different joints may be related to the angle between the joint and the incident load. The direction from the center of the structure to the joint is defined as the joint direction. The response of the lining structure was calculated under different conditions within the range of 0–90° of incidence angle in increments of 10°, and the relationship between the joint forces and the angle between the joint and the incident load was shown in Figure 10.

The peak value of the circumferential force of the joint reaches its minimum value when the angle between the joint and the incident load is 0°, and its maximum value when the angle is 90° in Figure 10(a). The relationship between the peak radial force of the joint and the angle between the joint and the incident load is approximately a sine curve with a period of π in Figure 10(b). When the angle between the joint and the incident load is 0°, the radial force peak value of the joint is around 0, and the radial force reaches its maximum value at ∼45°, 135°, 225°, and 315°. The relationship between the peak joint bending moment and the angle between the joint and incident load is approximately a cosine curve with a period of π in Figure 10(c). When the angle between the joint and incident load is 0° and 180°, the joint bending moment reaches its maximum positive value, and when it is 90° and 275°, the joint bending moment reaches its maximum negative value. Different from the joint circumferential and radial forces, the peak moment of the joint is not only related to the angle of the joint, but also to the size of the two segments of the joint. Joints 1 and 2, located on both sides of sealing rings with low mass, have a smaller peak moment than other joints when the angle between the joint and incident load is 0°.

The analysis in Figure 10 shows that the circumferential force of the joint is significantly greater than the bending moment and radial shear under the incident loads at different angles. This is due to the compressive stiffness of the joint being much larger than its shear and bending stiffness. Consequently, joint displacement caused by compression is considerably less than that caused by shear and bending. The sine and cosine functions can be used to determine the magnitude of bending moment and radial shear of the joint. In practical engineering, if the positions of different joints in the lining can be strategically arranged so that both the bending moment and shear force are minimized, the ability of the lining structure to resist incident loads can be improved.

4.4. Influence of Wavelength–Diameter Ratio. The wavelength of the incident load on the lining structure is half of the buried depth, h, and the rise time is one-third of the duration. According to Hao [19], tunnels in cities are usually shallow. Assuming that the buried depths of the lining are D, 1.5D, 2D, 2.5D, and 3D (where D is the outer diameter of the lining), the corresponding wavelength-to-diameter ratios, L/D, are 0.5, 0.75, 1, 1.25, and 1.5, respectively. Figure 11 shows the peak forces of the joints for the five different wavelength-to-diameter ratios.

It can be observed that the circumferential compression of joints 1 and 2 at both ends of the sealing ring is less sensitive to changes in the wavelength–diameter ratio when compared to the circumferential compression of joints 3–6 in Figure 11(a). Joints 4 and 5 have the highest peak value of radial force, and their value increases rapidly with the increase of wavelength–diameter ratio in Figure 11(b). On the other hand, joints 3 and 6 have the largest peak value of joint moment, and the peak value increases faster with the increase of the wavelength–diameter ratio than other joints in Figure 11(c). The above analysis reveals that the relationship between joint peak circumferential, radial shear force, and bending moment, and wavelength–diameter ratio is almost linear, indicating that the lining structure of shallow-buried tunnels operates in the pulse region or dynamic region when subjected to shock [21].

Since the force–time curves analysis of the joints and the large displacement gap observed under different wavelength–diameter ratios, the dimensionless treatment of the vertical displacement at the top of the lining and structural response time was conducted. The resulting time history curve of the displacement at the top of the lining is shown in Figure 12 for wavelength–diameter ratios of $L/D = 0.5$, 1, and 1.5. The actual vertical displacement peaks at the top of the lining for these three working conditions are 3.4, 5.8, and 8.5 mm, respectively.

Figure 11 illustrates that the maximum vertical displacement at the top of the lining occurred at 1.84, 1.18, and 1 times the load duration for the wavelength–diameter ratios of 0.5, 1, and 1.5, respectively. The corresponding actual times were 11.04, 15.34, and 20 ms, respectively. After reaching the peak value, the vertical displacement at the top of the lining remained unchanged for 6.7, 3.7, and 2.85 times the load duration, respectively. It can be observed from the time history curve for the wavelength–diameter ratio of 0.5 that the vertical displacement at the top of the structure continued to increase for a long time after the load ended, indicating that part of the vertical displacement at the top of the structure was caused by the inertial force.

The vertical displacement difference between the top and bottom of the lining is an important indicator to assess the deformation characteristics of the structure. To gain insights into the relationship between this displacement difference and the wavelength–diameter ratio of 0.5, 1, and 1.5, as

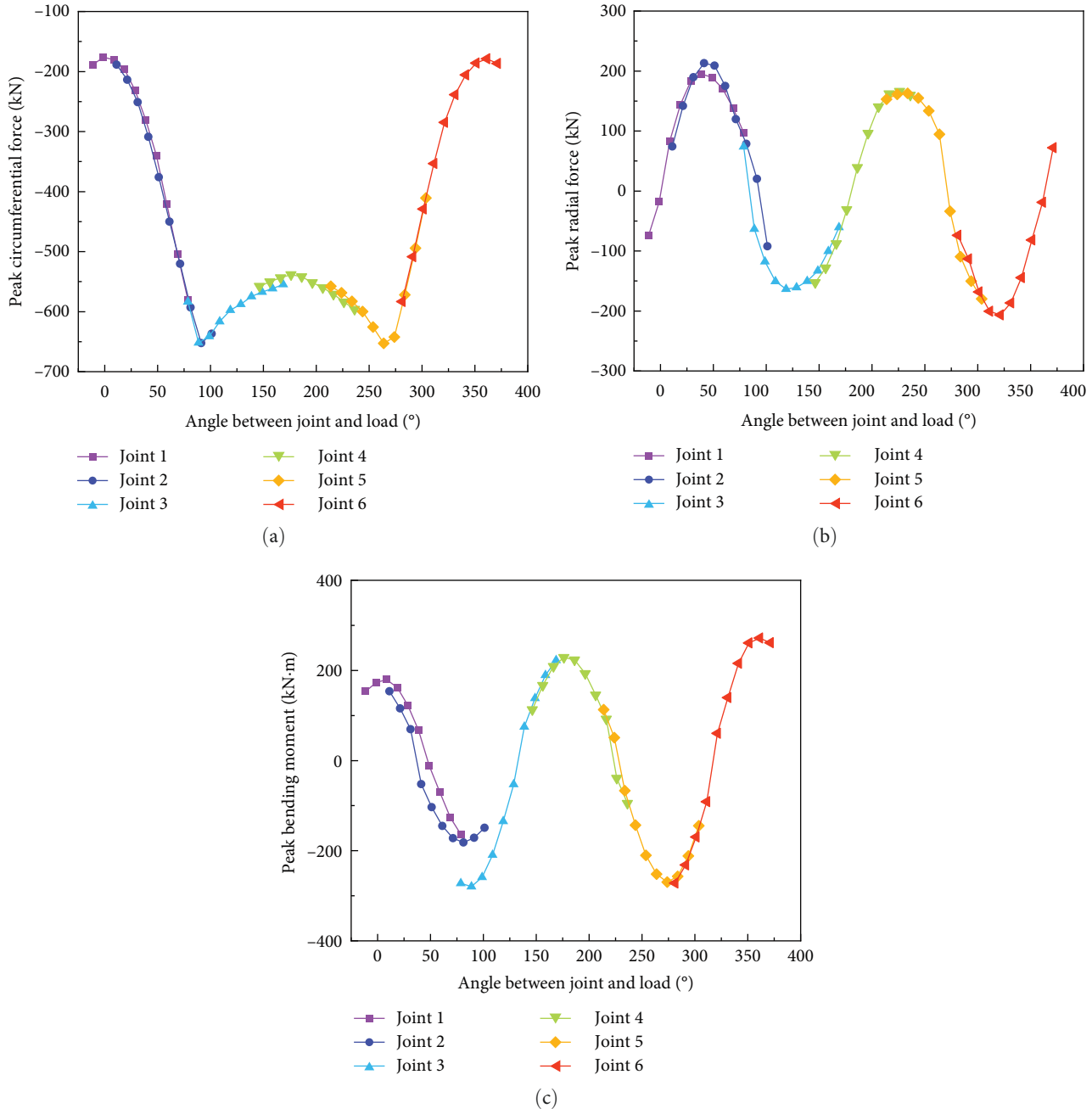

Figure 10: The influence of the angle between the joint and the incident load: (a) peak circumferential force of joints, (b) peak radial force of joints, and (c) peak bending moment of joints.

well as the dimensionless time, a graph was plotted in Figure 13. It can be observed from the graph that the time taken for the structure to reach the maximum vertical deformation is 1.65, 1.04, and 0.86 times the load duration for the wavelength–diameter ratio of 0.5, 1, and 1.5, respectively. Correspondingly, the actual time taken was 9.9, 13.52, and 17.2 ms, respectively. After reaching the maximum, the load duration remained unchanged at 6.78, 3.8, and 2.78 times for the three respective wavelength–diameter ratios.

It is worth noting that the maximum vertical deformation of the structure occurs at different times for different wavelength–diameter ratios, indicating that the deformation behavior of the structure varies under the different loads. Moreover, the maximum vertical displacement difference between the top and bottom of the lining is observed to increase with increasing wavelength–diameter ratio, which further indicates the influence of the load conditions on the deformation characteristics of the structure.

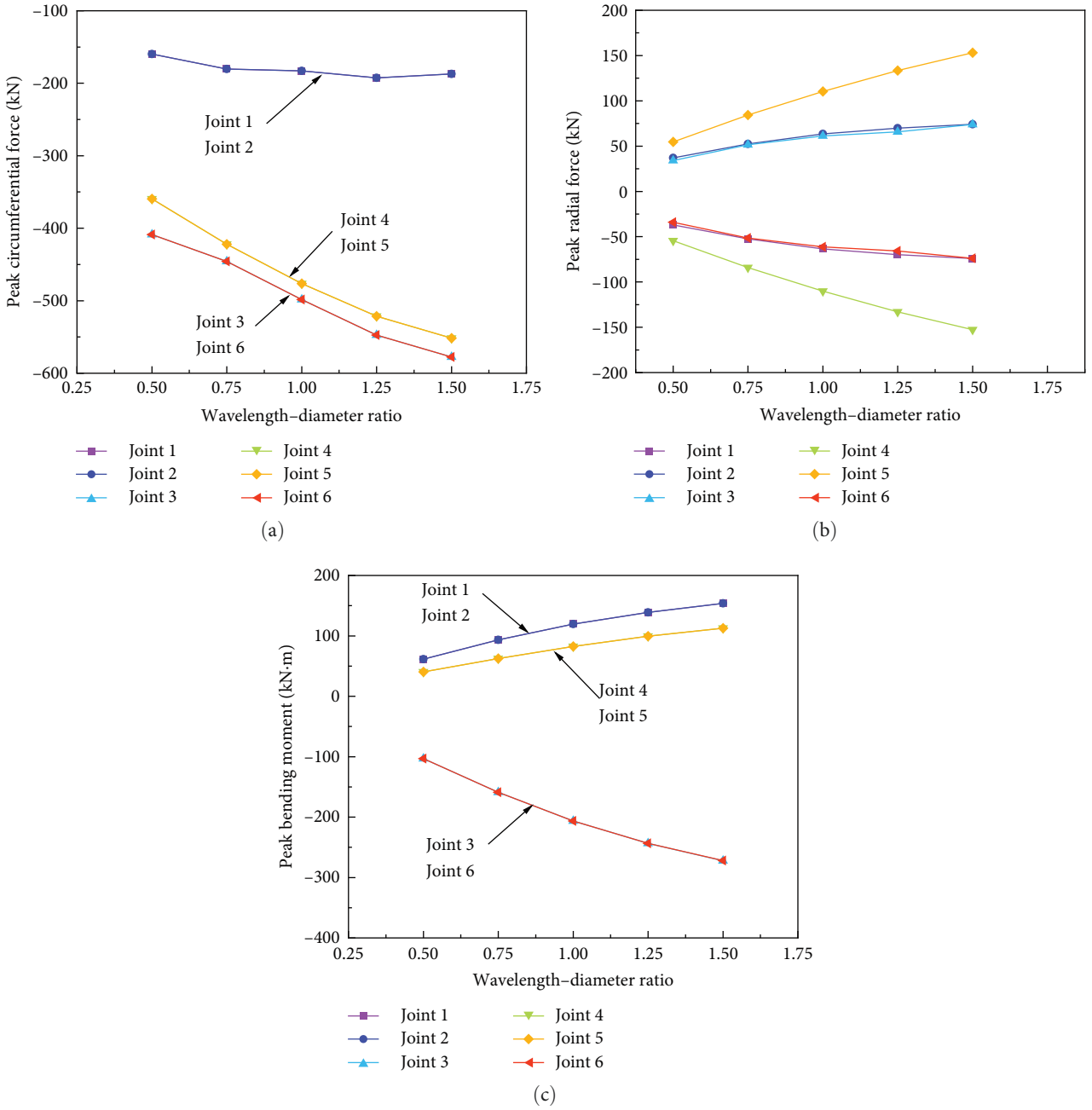

Figure 11: The relationship between the force of joints and the wavelength–diameter ratio: (a) peak circumferential force of joints, (b) peak radial force of joints, and (c) peak bending moment of joints.

Additionally, the analysis reveals that the time for the vertical deformation to reach its maximum value decreases as the wavelength–diameter ratio increases. This indicates that the structural deformation is more rapid under the larger wavelength–diameter ratios, which may have implications for the design and construction of shallow buried tunnels in urban areas. Furthermore, it is important to note that the peak value of displacement at the top of the structure and the peak value of vertical deformation are affected by various factors such as the depth of burial, the stiffness of the lining, and the characteristics of the incident loads. Therefore, a comprehensive understanding of these factors is crucial for the accurate prediction and control of structural deformation in shallow buried tunnels.

The analysis presented in Figures 12 and 13 provides valuable insights into the deformation behavior of shallow buried tunnel structures under different working conditions. These insights can be used to optimize the design and construction of such structures and enhance their ability to withstand the external loads.

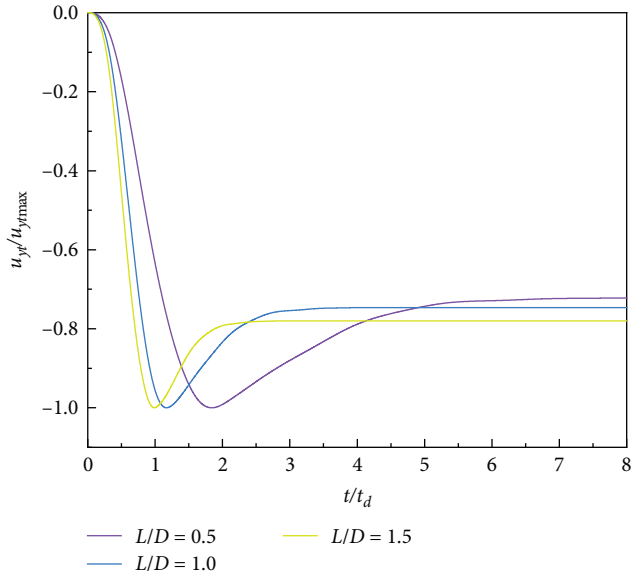

Figure 12: Dimensionless time history curve of the lining vertical displacement.

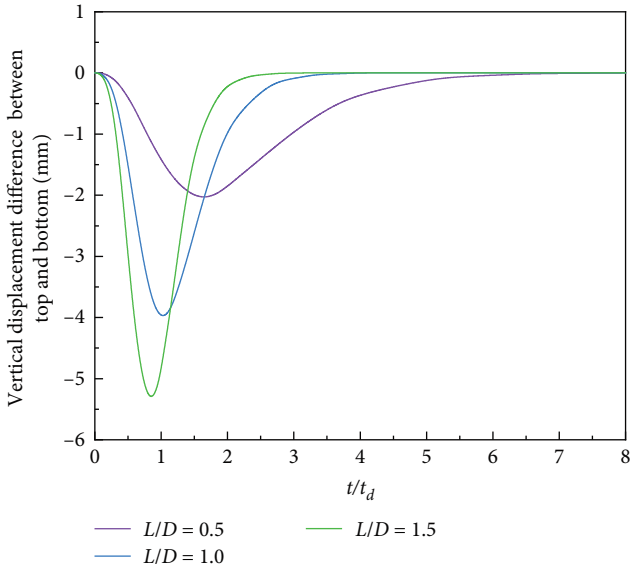

Figure 13: Dimensionless time history curve of vertical deformation of lining structure.

5. Conclusion

In this paper, a simplified calculation method for the dynamic response of segmental tunnel lining structures under the ground shock was proposed, and an analysis of an actual structure was carried out. The main conclusions are as follows:

(1) The segments of the tunnel lining were simplified into rigid bodies, and the dynamic equations of segments were established considering the tensile, compressive, shear, bending capacity of joints, and the interaction between the structure and the surrounding soil. The forces of the joints were in good agreement with the finite element calculation results, which verified the correctness of the simplified algorithm and calculation program.

(2) It was found that the trigonometric function can be used to determine whether the bending moment and radial shear of the joint are larger or smaller. If the positions of different joints in the lining can be set reasonably, so that the bending moment and shear force are in a small working condition, the anti-incident load ability of the lining structure can be improved to a certain extent.

(3) The results showed that the lining structure of shallow buried tunnels is in the pulse and dynamic region under the shock. With the increase of the wavelength–diameter ratio, the peak displacement and vertical deformation at the top of the structure increase obviously, and the proportion of the displacement and deformation caused by the inertia force decreases gradually. Therefore, it is important to consider the wavelength–diameter ratio when designing tunnel lining structures to ensure their stability and safety under the ground shock.

(4) In summary, the proposed simplified calculation method and the obtained results provide a valuable reference for the design and analysis of segmental tunnel lining structures under the ground shock.

Data Availability

The data used to support the findings of this study are included within the article.

Conflicts of Interest

The authors declare that they have no conflicts of interest.

Acknowledgments

This study is financially supported by Henan Provincial Department of Transportation, 2018J3 and Henan Provincial Department of Education, 23A580005.

References

[1] L. Ganbin, Z. Rongyue, and Z. Ye, "Numerical model for dynamic response of tunnel in clay under explosive loading," *Journal of Ningbo University Natural Science and Engineering*, vol. 22, no. 2, pp. 263–267, 2009.

[2] L. Muyu and L. Zhifang, "Analysis of dynamic response of yangtze river tunnel subjected to contact explosion loading," *Journal of Wuhan University of Technology*, vol. 01, pp. 113–117, 2007.

[3] Y. Yang, X. Xie, and R. Wang, "Numerical simulation of dynamic response of operating metro tunnel induced by ground explosion," *Journal of Rock Mechanics and Geotechnical Engineering*, vol. 2, no. 4, pp. 373–384, 2010.

[4] A. Rashiddel, M. Kharghani, D. Dias, and M. Hajihassani, "Numerical study of the segmental tunnel lining behavior under a surface explosion-impact of the longitudinal joints

shape," *Computers and Geotechnics*, vol. 128, Article ID 103822, 2020.
[5] A. De, A. Niemiec, and T. F. Zimmie, "Physical and numerical modeling to study effects of an underwater explosion on a buried tunnel," *The Journal of Geotechnical and Geoenvironmental Engineering*, vol. 143, no. 5, Article ID 04017002, 2017.
[6] N. A. Do, *Numerical Analyses of Segmental Tunnel Lining Under Static and Dynamic Loads*, INSA, Lyon, 2014.
[7] C. B. M. Blom, *Design Philosophy of Concrete Linings for Tunnels in Soft Soils*, Technical Univercity of Delft, DUP Science, Delft, Netherlands, 2000.
[8] H. H. Zhu, "*Designs and analysis on underground structures*, Geo-research Institute Report," Osaka, Japan, 1995.
[9] W. Q. Ding, Z. Q. Yue, L. G. Tham, H. H. Zhu, C. F. Lee, and T. Hashimoto, "*Anal*ysis of shield tunnel," *International Journal for Numerical and Analytical Methods in Geomechanics*, vol. 28, no. 1, pp. 57–91, 2004.
[10] K. Lee and X. Ge, "The equivalence of a jointed shield-driven tunnel lining to a continuous ring structure," *Canadian Geotechnical Journal*, vol. 38, no. 3, pp. 461–483, 2001.
[11] K. M. Lee, X. Y. Hou, X. W. Ge, and Y. Tang, "An analytical solution for a jointed shield-driven tunnel lining," *International Journal for Numerical and Analytical Methods in Geomechanics*, vol. 25, no. 4, pp. 365–390, 2001.
[12] N.-A. Do, D. Dias, P. Oreste, and I. Djeran-Maigre, "2D numerical investigation of segmental tunnel lining behavior," *Tunnelling and Underground Space Technology*, vol. 37, pp. 115–127, 2013.
[13] Y. Karinski and D. Yankelevsky, "Dynamic analysis of an elastic–plastic multisegment lining buried in soil," *Engineering Structures*, vol. 29, no. 3, pp. 317–328, 2007.
[14] Y. Karinski, V. Feldgun, and D. Yankelevsky, "Shock waves interaction with a single inclusion buried in soil," *International Journal of Impact Engineering*, vol. 45, pp. 60–73, 2012.
[15] Y. Liu, M. Wang, J. Li, D. Wang, and N. Zhang, "Analysis of dynamic response of shield tunnel to explosion seismic wave," *Rock and Soil Mechanics*, vol. 35, no. 4, pp. 1056–1062 1068, 2014.
[16] Z. Luo, *Theoretical Analysis and Experimental Study on Resistance to Internal Explosion of Segment Structure of Cross-River Tunnel*, PLA University of Science and Technology, Nanjing, 2012.
[17] A. De, A. Niemiec, and T. F. Zimmie, "Physical and numerical modeling to study effects of an underwater explosion on a buried tunnel," *Geotechnical and Geological Engineering*, vol. 143, no. 5, Article ID 04017002, 2017.
[18] S. Liu, K. Feng, C. He, and Z. S. He, "Study on the bending mechanical model of segmental joint in shield tunnel with large cross-section," *Engineering Mechanics*, vol. 32, no. 12, pp. 215–224, 2015.
[19] B. Hao, *Underground Nuclear Explosion and Its Application*, National Defense Industry Press, Beijing, 2002.
[20] E. C. Leong, S. Anand, H. K. Cheong, and C. H. Lim, "Re-examination of peak stress and scaled distance due to ground shock," *International Journal of Impact Engineering*, vol. 34, no. 9, pp. 1487–1499, 2007.
[21] T. Krauthammer, *Modern Protective Structures*, CRC Press, 2008.